Thickness Evaluation of Hollow Nonmagnetic Cylinders Utilizing Motional Eddy Current

Mehran Mirzaei, Pavel Ripka, Vaclav Grim, Lukas Jelinek and Jakub Svatos

Faculty of Electrical Engineering, Czech Technical University, Prague 16627, Czech Republic
(e-mails: mirzameh@fel.cvut.cz)

***Abstract*—This paper presents the shell thickness calculation of nonmagnetic hollow cylinders for nondestructive applications. Aluminum cylinders with a solid structure and hollow structure are considered. The motion component of induced eddy currents in the conductive cylinder is utilized to evaluate the shell thickness of the hollow conductive cylinders at different frequencies and variable speeds. One axisymmetric excitation coil and two axisymmetric pickup coils with antiserially connection are used. An analytical method using axisymmetric computational model is developed for parametric analysis of solid and hollow cylinder structures and shell thickness calculations, which Fourier series are utilized. 2D axisymmetric finite element method is also performed for comparison with analytical method results. The measurements at variable speeds and different frequencies are presented with different hollow aluminum cylinders. The high linearity of induced voltage versus speed curve makes it possible to calculate the shell thickness of nonmagnetic hollow cylinders at different speeds.**

***Keywords*— Moving conductive cylinders, aluminum, motional eddy current, speed, nondestructive, analytical, 2D FEM.**

I. Introduction

The safety and quality evaluations in different branches of industrial and civil applications are always in increasing demand. Metals with ferromagnetic and non-ferromagnetic materials are used as a skeleton in many apparatuses. Several non-destructive methods, for example, radiographic testing, visual testing, ultrasonic testing, magnetic particle testing, liquid penetrant testing, magnetic flux linkage, electromagnetic testing, vibration testing, and thermal testing are utilized for safety and quality assessments of metals with a plate and cylindrical configurations. Nondestructive testing (NDT) based on eddy current testing (ECT) is a well-known method of electromagnetic testing, which several magnificent works were done and published in this field [1].

Multi-frequency eddy current sensor was used with high immunity to liftoff error for measurement of nonmagnetic plate thickness in [2], in which peak frequency of imaginary part of difference inductance is inversely proportional to plate thickness. A similar methodology as [2] was presented in [3] using a triple coil. A combined inductive and capacitive sensor with compensating liftoff effect was used in [4] with single frequency for nonmagnetic plate thickness measurement. A pulsed source was used for thickness evaluation of ferromagnetic plate in [5] and [6], which claimed better performance than a harmonic source. Thickness measurement of the nonmagnetic plate was presented in [7] using the skin effect method, which show low error concerning the liftoff effect for thickness estimation. Multifrequency technique was also used in [8] for thickness evaluation of small diameter copper disc. All results in [2]-[8] were presented for static conditions without motion consideration.

Using the swept-frequency method was applied in [9] for thickness measurement of nonmagnetic and ferromagnetic pipes. Pulsed eddy current sensor and testing method were used for thickness measurements of pipes in [10] and [11]. Using multi-frequency method and pulsed method mentioned in [9]-[11] for pipes with radial direction measurement using parallel coils cannot correctly estimate hollow cylinder shell thickness in 360 degrees (as pipe is different with plate) at single position of coils and the measurement coils need to be rotated in angular direction to cover 360 degrees. Therefore, angular speed effects in high speed measurements need to be considered along with speed effects in longitudinal direction. And also, they presented for large diameter pipes, which is easier to measure than small hollow cylinders. The static methods are suitable for short length cylinder or for short length of a cylinder. Inspection of outer side defect in steel tube with DC bias method was developed in [12], which can be utilized for shell thickness evaluation of magnetic steel pipes. However, speed effects on the measurements was not mentioned. No experimental and theoretical works were published and reported on measurement of shell thickness of nonmagnetic hollow cylinders or pipes according to the authors' knowledge with taking into account the speed effects of induced eddy current.

Utilizing the motional component of an induced eddy current in the conductive moving objects is as longstanding as the Faraday generator and the unipolar generator. However, it has still countless attentions in the applications and theoretical analysis [13] perspectives. For example, the effects of the motional component or speed effects of induced eddy current for NDT were presented and evaluated in [14]-[20], which are inevitable in NDT. It was shown that speed effects could create non-negligible errors.

The motional component of induced eddy current is used for magnetic flowmeter in [21] using the finite difference method at constant fluid speed. And also, its utilization in the solid conductive bodies was only investigated for thickness evaluation of plates in [22]-[24] at various constant speeds. The eddy current speed sensor for speed measurements of solid magnetic and nonmagnetic objects was presented in [25]-[27] at time varying speeds.

An axisymmetric linear speed sensor with one excitation coil and two antiserially connected pickup coils is constructed to measure induced voltage in the pickup coils proportional to the relative speed of the pickup coils and cylinders. First operational performance of the speed sensor is presented and then evaluation of shell thickness of aluminum hollow cylinders with outer diameter 20 mm is shown in this paper at variable speeds and different excitation frequencies. Speed effects in a solid aluminum cylinder and solid brass cylinder are also investigated to compare with a hollow cylinder and evaluate material effects in nonmagnetic cylinders. The analytical analysis using the method of separation of variables is applied to analyze the speed effects of induced eddy current. Approach using Fourier series is preferable over method with Fourier transform [23]-[24], [27]-[28] to avoid complicated integration and find closed-form formulas. The analytical method is more suitable in comparison with numerical finite difference [21] and finite element methods for parametric and fast analyses. Also, an 18 mm hollow cylinder with a 2 mm shell thickness is studied to assess the effects of eccentricity or misalignment between sensor coils and moving cylinder.

II. Structure and Operation Theory

The moving cylinder and excitation coil between two antiserillay connected pickup coils are shown in Fig. 1. It is considered that the cylinder is moving, and the coils are stationary, although vice versa is more practical. Nevertheless, the relative speed between the cylinder and the coils is important for the analysis.

The induced voltage in antiserially connected pickup coils is zero when relative speed is zero. As the flux linkages in both pickup coils are the same, which induces the same amount of voltage. The induced voltage deviates from zero to negative or positive values depending on speed motion direction when relative speed is nonzero for the reason that the flux linkage and induced in each pickup coil are unequal according to Fig. 2.

Tables 1 and 2 present the moving cylinders and the parameters and dimensions of the coil. The total axial length of the sensor (excitation coil + pick up coils) is 63.2 mm. The wire diameter of the coils is 0.1 mm.

Table 1
Parameters of excitation coil, pickup coils arrangement and moving cylinders

Parameters		Values
I	excitation coil current amplitude	169 mA
N_e	number of turns in excitation coil	100
N_p	number of turns in each pickup coil	50
h_e	excitation coil height	30.6 mm
h_p	each pickup coil height	15.3 mm
d	excitation coil and pickup coil distance	1 mm
r_w	mean radius of coils	10.8 mm
r_o	the outer radius of the solid or hollow cylinder	10.0 mm
r_i	the inner radius of the hollow cylinder	-
d_c	the thickness of the hollow cylinder	r_o -r_i

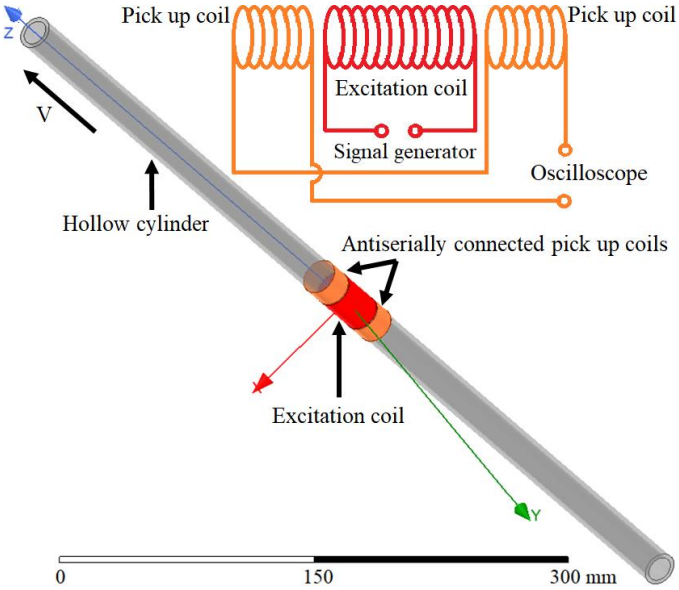

Fig. 1. 3D model of excitation coil and antiserially connected pickup coils arrangement (sensor) with moving hollow cylinder and wiring diagram

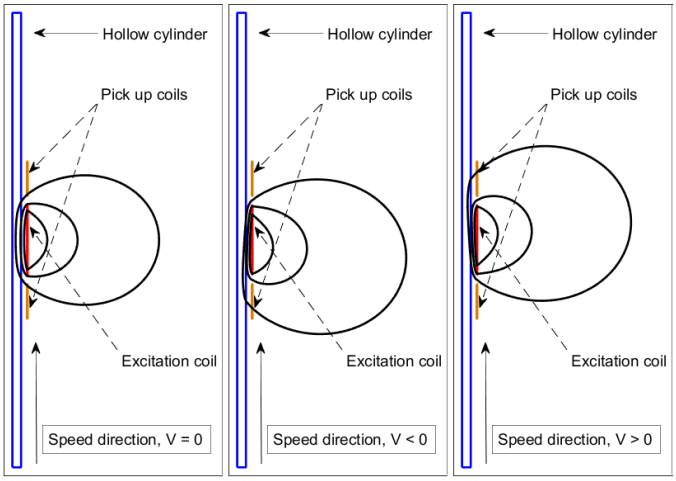

Fig. 2. Schematic magnetic flux distribution depicting speed effects

Table 2
Measured electrical conductivity for solid brass and aluminum cylinders and hollow aluminum cylinders

Cylinder	Conductivity	Cylinder	Conductivity
Solid brass	15.0 MS/m	Hollow aluminum, d_c=2.0 mm	29.175 MS/m
Solid aluminum	28.54 MS/m	Hollow aluminum, d_c=1.5 mm	32.48 MS/m
Hollow aluminum, d_c=5.0 mm	30.17 MS/m	Hollow aluminum, d_c=1.0 mm	31.77 MS/m

III. Modeling

The source fields caused by excitation coil and reaction fields

caused by induced eddy current in the cylinders are separated in the analytical modeling to simplify calculations. Firstly, source fields are obtained in the primary phase. Secondly, reaction fields are calculated in the next phase using source fields obtained in the first phase.

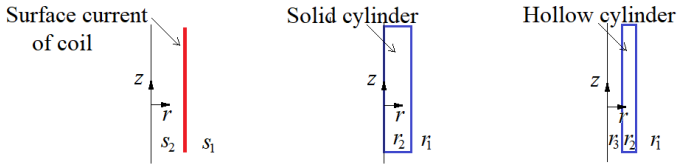

Fig. 3. 2D axisymmetric computational model in *r*-*z* coordinate – Model for only coil (left) with two regions, s_1 and s_2, model for solid cylinder (middle) with two regions, r_1 and r_2 and model for hollow cylinders, r_1, r_2 and r_3 (right)

A. *Source Fields Caused by Excitation Coil*

The first step, only the magnetic fields generated by the coils is modeled and the reaction magnetic fields are skipped. The thin coils regions are replaced with the line region and the excitation coil volume is replaced with an equivalent cylindrical surface current source. The obtained partial differential equations in cylindrical coordinate are presented in (1) corresponding to two regions s_1 and s_2 (Fig. 3). The regions s_1 and s_2 correspond to the air parts outside and inside of the equivalent surface current source in the computational model, respectively. The final differential equations in (1) have the only azimuthal-angle component of the magnetic vector potential, $A_\emptyset$ as the model has axisymmetric configuration and the 3D model (Appendix) can be simplified to the 2D model [28]. Therefore, magnetic flux density and magnetic field strength have only radial and axial components, B_r, B_z, H_r, and H_z, respectively.

$$\frac{1}{r}\frac{\partial}{\partial r}\left(r\frac{\partial A_{\emptyset,s_1}}{\partial r}\right)+\frac{\partial^2 A_{\emptyset,s_1}}{\partial z^2}-\frac{A_{\emptyset,s_1}}{r^2}=0$$
$$\frac{1}{r}\frac{\partial}{\partial r}\left(r\frac{\partial A_{\emptyset,s_2}}{\partial r}\right)+\frac{\partial^2 A_{\emptyset,s_2}}{\partial z^2}-\frac{A_{\emptyset,s_2}}{r^2}=0 \quad (1)$$

To solve (1) analytically, the method of separation of variables (method of Fourier) is used [25]-[26] and [29]. Two assumptions are considered for the method of separation of variables: 1- Magnetic fields change is sinus function versus time as source current is sinusoidal. 2- It is also assumed that magnetic sensor model is artificially repeating with period 2*L* in axial direction (z-axis), and it is a symmetric function in period 2*L*. Therefore, magnetic fields change is periodic sinus functions with odd order harmonic numbers (±1, ±3, …) in the z-direction with period length, 2*L*. The length, *L* must be considered enough large to take into account the end effects caused by motional component of induced eddy currents, which is related to the effects of finite axial length of the excitation coil. *L* is equal to the axial length of cylinder, 700 mm in this paper, which is large enough for the sensor model.

Therefore, derivations in (1) could be replaced as follows:

$$A_\emptyset = R(r)\cdot Z(z)\cdot T(t)$$
$$Z(z)\propto e^{-jm\cdot z}, m=\frac{n\pi}{L}, n=\pm1,\pm3,\cdots$$
$$\frac{\partial A_\emptyset}{\partial z}=-jm\cdot A_\emptyset,\ \frac{\partial^2 A_\emptyset}{\partial z^2}=-m^2\cdot A_\emptyset$$
$$T(t)\propto e^{j\omega\cdot t},\ \frac{\partial A_\emptyset}{\partial t}=j\omega\cdot A_\emptyset, \omega=2\pi f \quad (2)$$

where, f is the frequency in Hz.

Therefore, differential equations in (1) can be calculated versus radial position, *r*. using Bessel functions. The solutions of (1) using (2) versus time, *t*, axial position, *z* and radial position, *r* are presented in (3):

$$A_{\emptyset,s_1}=\sum_{n=\pm1,\pm3,\ldots}\left(C_{1,s_1}\cdot \mathrm{I}_1(|m|r)+C_{2,s_1}\cdot \mathrm{K}_1(|m|r)\right)e^{j(\omega t-mz)}$$
$$A_{\emptyset,s_2}=\sum_{n=\pm1,\pm3,\ldots}\left(C_{1,s_2}\cdot \mathrm{I}_1(|m|r)+C_{2,s_2}\cdot \mathrm{K}_1(|m|r)\right)e^{j(\omega t-mz)} \quad (3)$$

where I_1 and K_1 are Bessel functions of the first order. C_1'sand C_2's are constants, which are calculated using the following boundary conditions between regions s_1 and s_2:

$$A_{\emptyset,s_1}(r=\infty)=0$$
$$B_{r,s_1}(r=r_w)=B_{r,s_2}(r=r_w),$$
$$H_{z,s_1}(r=r_w)-H_{z,s_2}(r=r_w)=J_{\emptyset,S}$$
$$A_{\emptyset,s_2}(r=0)=0 \quad (4)$$

Parameter $J_{\emptyset,S}$ in (4) is azimuthal surface current density equivalent to the excitation coil current and it could be calculated as follows:

$$J_{\emptyset,S}=\sum_n J_{s,n},\ J_{s,n}=\frac{2}{n\pi}\cdot\sin\left(m\cdot\frac{h_e}{2}\right)\cdot J_s,\ J_s=\frac{N_e I}{h_e} \quad (5)$$

where J_s is the line current density in the excitation coil. The constants using (4) and (5) are calculated in (6).

$$C_{1,s_1}=0$$
$$C_{2,s_1}=\frac{\mu_0\cdot J_{s,n}}{|m|\cdot\left(\frac{\mathrm{I}_0(|m|\cdot r_w)}{\mathrm{I}_1(|m|\cdot r_w)}\mathrm{K}_1(|m|\cdot r_w)+\mathrm{K}_0(|m|\cdot r_w)\right)}$$
$$C_{2,s_2}=0$$
$$C_{1,s_2}=\frac{\mu_0\cdot J_{s,n}}{|m|\cdot\left(\mathrm{I}_0(|m|\cdot r_w)+\frac{\mathrm{K}_0(|m|\cdot r_w)}{\mathrm{K}_1(|m|\cdot r_w)}\mathrm{I}_1(|m|\cdot r_w)\right)} \quad (6)$$

The self-inductance of excitation coil, L_s is calculated as follows using calculating excitation coil flux linkage, Ψ_s (integration is applied on coil surface in azimuthal direction):

$$L_s = \frac{\Psi_s}{I} = \frac{N_e \int A_\phi dS}{I h_e} = N_e \sum_{n=\pm1,\pm3,\ldots} C_{2,s_1} \cdot \mathrm{K}_1(|m| \cdot r_w) \frac{4\pi}{m} \sin\left(m\frac{h_e}{2}\right) \frac{r_w}{h_e I} \quad (7)$$

Table 3 compares the analytical calculation of self-inductance of the excitation coil in comparisons with measured inductance using LCR meter, HAMAG, HM818, which shows the high accuracy of analytical modeling with only 0.35% error.

Table3
Excitation coil inductance with air core

Experimental	Analytical using equation (7)
113.9 μH (100.00%)	114.3 µH (100.35%)

B. Reaction Fields Caused by Induced Eddy Currents in Conductive Cylinder

Three regions, r_1, r_2, and r_3 are considered to calculate reaction fields in hollow cylinder case (Fig. 3). Regions r_1, r_2, and r_3 correspond to the air part outside the hollow cylinder and conductive part of the hollow cylinder and air part inside the hollow cylinder, respectively.

The partial differential equations are presented for three regions in (8). The differential equation in (8) corresponding to the region, r_2 $\left(A_{\emptyset,r_2}\right)$ has two components of induced eddy currents in right-hand side of equation. First term is transformer component of induced eddy current and second term is motional component of induced eddy current, which is proportional to the speed, V.

$$\begin{gathered}\frac{1}{r}\frac{\partial}{\partial r}\left(r\frac{\partial A_{\emptyset,r_1}}{\partial r}\right) + \frac{\partial^2 A_{\emptyset,r_1}}{\partial z^2} - \frac{A_{\emptyset,r_1}}{r^2} = 0 \\ \frac{1}{r}\frac{\partial}{\partial r}\left(r\frac{\partial A_{\emptyset,r_2}}{\partial r}\right) + \frac{\partial^2 A_{\emptyset,r_2}}{\partial z^2} - \frac{A_{\emptyset,r_2}}{r^2} \\ = \sigma\mu_0\frac{\partial A_{\emptyset,r_2}}{\partial t} + V\sigma\mu_0\frac{\partial A_{\emptyset,r_2}}{\partial z} \\ \frac{1}{r}\frac{\partial}{\partial r}\left(r\frac{\partial A_{\emptyset,r_3}}{\partial r}\right) + \frac{\partial^2 A_{\emptyset,r_3}}{\partial z^2} - \frac{A_{\emptyset,r_3}}{r^2} = 0\end{gathered} \quad (8)$$

where, μ_0 and σ are vacuum magnetic permeability and electrical conductivity, respectively. The solutions of (8) are presented in (9).

$$\begin{aligned}A_{\emptyset,r_1} &= \sum_{n=\pm1,\pm3,\ldots} \left(C_{1,r_1} \cdot \mathrm{I}_1(|m|r) + C_{2,r_1} \cdot \mathrm{K}_1(|m|r)\right) e^{j(\omega t - mz)} \\ A_{\emptyset,r_2} &= \sum_{n=\pm1,\pm3,\ldots} \left(C_{1,r_2} \cdot \mathrm{J}_1(\gamma r) + C_{2,r_2} \cdot \mathrm{Y}_1(\gamma r)\right) e^{j(\omega t - mz)} \\ A_{\emptyset,r_3} &= \sum_{n=\pm1,\pm3,\ldots} \left(C_{1,r_3} \cdot \mathrm{I}_1(|m|r) + C_{2,r_3} \cdot \mathrm{K}_1(|m|r)\right) e^{j(\omega t - mz)}\end{aligned} \quad (9)$$

where J_1 and Y_1 are Bessel functions of the first order. The boundary conditions in (10) are used to calculate constants C_1's and C_2's in (9) [29]. B_{r,s_1} and H_{z,s_1} in (10) are a radial component of source magnetic flux density and axial component of source magnetic field strength, which are calculated from (3). Therefore, the constants in (9) are calculated in (11) - (13).

$$\begin{gathered}A_{\emptyset,r_1}(r=\infty) = 0 \\ B_{r,r_1}(r=r_o) + B_{r,s_1}(r=r_o) = B_{r,r_2}(r=r_o), \\ H_{z,r_1}(r=r_o) + H_{z,s_1}(r=r_o) = H_{z,r_2}(r=r_o) \\ B_{r,r_2}(r=r_i) = B_{r,r_3}(r=r_i), \\ H_{z,r_2}(r=r_i) = H_{z,r_3}(r=r_i) \\ A_{\emptyset,r_3}(r=0) = 0\end{gathered} \quad (10)$$

$$C_{1,r_1} = 0$$

$$C_{2,r_1} = \frac{C_{1,s_2} \cdot \left(\frac{|m|}{\gamma} \cdot \frac{\mathrm{I}_0(|m| \cdot r_o)}{D_2} - \frac{\mathrm{I}_1(|m| \cdot r_o)}{D_3}\right)}{\frac{|m|}{\gamma} \cdot \frac{\mathrm{K}_0(|m| \cdot r_o)}{D_2} + \frac{\mathrm{K}_1(|m| \cdot r_o)}{D_3}} \quad (11)$$

$$C_{1,r_2} = \frac{C_{1,s_2} \cdot \frac{|m|}{\gamma} \cdot \left(\frac{\mathrm{I}_0(|m| \cdot r_o)}{\mathrm{K}_0(|m| \cdot r_o)} + \frac{\mathrm{I}_1(|m| \cdot r_o)}{\mathrm{K}_1(|m| \cdot r_o)}\right)}{\frac{D_2}{\mathrm{K}_0(|m| \cdot r_o)} + \frac{|m|}{\gamma} \cdot \frac{D_3}{\mathrm{K}_1(|m| \cdot r_o)}}$$

$$C_{2,r_2} = D_1 \frac{C_{1,s_2} \cdot \frac{|m|}{\gamma} \cdot \left(\frac{\mathrm{I}_0(|m| \cdot r_o)}{\mathrm{K}_0(|m| \cdot r_o)} + \frac{\mathrm{I}_1(|m| \cdot r_o)}{\mathrm{K}_1(|m| \cdot r_o)}\right)}{\frac{D_2}{\mathrm{K}_0(|m| \cdot r_o)} + \frac{|m|}{\gamma} \cdot \frac{D_3}{\mathrm{K}_1(|m| \cdot r_o)}} \quad (12)$$

$$C_{1,r_3} = D_4 \frac{C_{1,s_2} \cdot \frac{|m|}{\gamma} \cdot \left(\frac{\mathrm{I}_0(|m| \cdot r_o)}{\mathrm{K}_0(\gamma \cdot r_o)} + \frac{\mathrm{I}_1(|m| \cdot r_o)}{\mathrm{K}_1(\gamma \cdot r_o)}\right)}{\frac{D_2}{\mathrm{K}_0(\gamma \cdot r_o)} + \frac{|m|}{\gamma} \cdot \frac{D_3}{\mathrm{K}_1(\gamma \cdot r_o)}}$$

$$C_{2,r_3} = 0 \quad (13)$$

The constants D_1, D_2, D_3 and D_4 in (11)-(13) are presented in (14).

$$\begin{gathered}D_1 = \frac{\mathrm{J}_1(\gamma \cdot r_i) - \frac{\gamma}{|m|} \cdot \frac{\mathrm{I}_1(|m| \cdot r_i)}{\mathrm{I}_0(|m| \cdot r_i)} \mathrm{J}_0(\gamma \cdot r_i)}{\frac{\gamma}{|m|} \cdot \frac{\mathrm{I}_1(|m| \cdot r_i)}{\mathrm{I}_0(|m| \cdot r_i)} \mathrm{Y}_0(\gamma \cdot r_i) - \mathrm{Y}_1(\gamma \cdot r_i)} \\ D_2 = \mathrm{J}_0(\gamma \cdot r_o) + D_1 \cdot \mathrm{Y}_0(\gamma \cdot r_o) \\ D_3 = \mathrm{J}_1(\gamma \cdot r_o) + D_1 \cdot \mathrm{Y}_1(\gamma \cdot r_o) \\ D_4 = \frac{J_1(\gamma \cdot r_i) + D_1 \cdot Y_1(\gamma \cdot r_i)}{\mathrm{I}_1(|m| \cdot r_i)}\end{gathered} \quad (14)$$

The constants are simplified for the case of solid cylinder in

(15) and (16) for regions, r_1 and r_2:

$$C_{1,r_1} = 0$$
$$C_{2,r_1} = \frac{C_{1,s_2} \cdot \left(\frac{|m|}{\gamma} \cdot \frac{\mathrm{I}_0(|m| \cdot r_o)}{\mathrm{J}_0(\gamma \cdot r_o)} - \frac{\mathrm{I}_1(|m| \cdot r_o)}{\mathrm{J}_1(\gamma \cdot r_o)}\right)}{\frac{|m|}{\gamma} \cdot \frac{\mathrm{K}_0(|m| \cdot r_o)}{\mathrm{J}_0(\gamma \cdot r_o)} + \frac{\mathrm{K}_1(|m| \cdot r_o)}{\mathrm{J}_1(\gamma \cdot r_o)}}$$

(15)

$$C_{2,r_2} = 0$$
$$C_{1,r_2} = \frac{C_{1,s_2} \cdot \frac{|m|}{\gamma} \cdot \left(\frac{\mathrm{I}_0(|m| \cdot r_o)}{\mathrm{K}_0(|m| \cdot r_o)} + \frac{\mathrm{I}_1(|m| \cdot r_o)}{\mathrm{K}_1(|m| \cdot r_o)}\right)}{\frac{\mathrm{J}_0(\gamma \cdot r_o)}{\mathrm{K}_0(|m| \cdot r_o)} + \frac{|m|}{\gamma} \cdot \frac{\mathrm{J}_1(\gamma \cdot r_o)}{\mathrm{K}_1(|m| \cdot r_o)}}$$

(16)

$$C_{1,r_3} = 0$$
$$C_{2,r_3} = 0$$

(17)

C. *Induced Voltage*

The total induced voltage in each pick up coil, $U_{U,L}$ (upper (U) and Lower (L)) consists of two components:

$$U_{U,L} = U_{U,L-s} + U_{U,L-r}$$

(18)

where, $U_{U,L\text{-}s}$ and $U_{U,L\text{-}r}$ are induced voltages in pick up coils caused by source fields and reaction fields of induced eddy currents in conductive cylinder, respectively.

The induced voltage of antiserially connected pickup coils caused by source fields, U_{d-s} are calculated as follows:

$$\Psi_{U,L-s} = \frac{N_p \int A_{\phi,s} dS}{h_p},\ \Psi_{d-s} = \Psi_{U-s} - \Psi_{L-s},$$
$$U_{d-s} = U_{U-s} - U_{L-s}$$
$$= -\frac{d\Psi_{d-s}}{dt} = -j\omega\Psi_{d-s},$$

(19)

$$\Psi_{U-s} = N_p \sum_{n=\pm1,\pm3,\ldots} C_{2,s_1} \cdot C_\Psi \cdot e^{-jm\left(\frac{h_e}{2}+d+\frac{h_p}{2}\right)}$$

(20)

$$\Psi_{L-s} = N_p \sum_{n=\pm1,\pm3,\ldots} C_{2,s_1} \cdot C_\Psi \cdot e^{jm\left(\frac{h_e}{2}+d+\frac{h_p}{2}\right)}$$

(21)

$$C_\Psi = \mathrm{K}_1(|m| \cdot r_w) \frac{4\pi}{m} \sin\left(m\frac{h_p}{2}\right) \frac{r_w}{h_p}$$

(22)

$$U_{d-s} = U_{U-s} - U_{L-s} = -j\omega N_p \sum_{n=\pm1,\pm3,\ldots} C_{2,s_1}$$
$$\cdot C_\Psi \cdot \sin\left(m\left(\frac{h_e}{2} + d + \frac{h_p}{2}\right)\right)$$

(23)

The same procedure is used to calculate induced voltage of antiserially connected pickup coils caused by reaction fields, U_{d-r}:

$$\Psi_{U-r} = N_p \sum_{n=\pm1,\pm3,\ldots} C_{2,r_1} \cdot C_\Psi \cdot e^{-jm\left(\frac{h_e}{2}+d+\frac{h_p}{2}\right)}$$

(24)

$$\Psi_{L-r} = N_p \sum_{n=\pm1,\pm3,\ldots} C_{2,r_1} \cdot C_\Psi \cdot e^{jm\left(\frac{h_e}{2}+d+\frac{h_p}{2}\right)}$$

(25)

$$U_{d-r} = U_{R-r} - U_{L-r} = -j\omega N_p \sum_{n=\pm1,\pm3,\ldots} C_{2,r_1}$$
$$\cdot C_\Psi \cdot \sin\left(m\left(\frac{h_e}{2} + d + \frac{h_p}{2}\right)\right)$$

(26)

Therefore, total differential voltage, U_d is calculated as follows:

$$U_d = U_{d-s} + U_{d-r}$$

(27)

Fig. 4 shows real and imaginary components of voltages of each pick up coil (U and L) caused by excitation coil and reaction fields of induced eddy current. Real and imaginary components of voltage are calculated or measured relative to excitation coil current as a reference signal. The pick coils voltages versus speed are the same for the excitation field. The pick coils voltages versus speed are different for the reaction field. Therefore, the differential voltage corresponding to the source field, $U_{d\text{-}s}$ is zero and total differential voltage, U_d is equal to $U_{d\text{-}r}$ in (27). The proposed sensor can measure speed and its direction as it is sensitive to motion polarity too.

The main advantages of two antiserially connected pick up coils to one single pick up coil (one receiver) are higher sensitivity and minimizing offset errors using differential voltage.

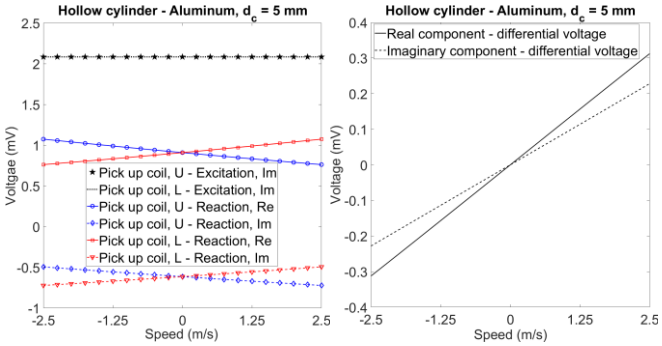

Fig. 4. Real (Re) and imaginary (Im) components of voltages for upper (U) pick up coil and lower (L) pick up coil versus speed, which generated by excitation fields and reaction fields of induced eddy current (left) and their differential voltage (right) – 170 Hz (Analytical)

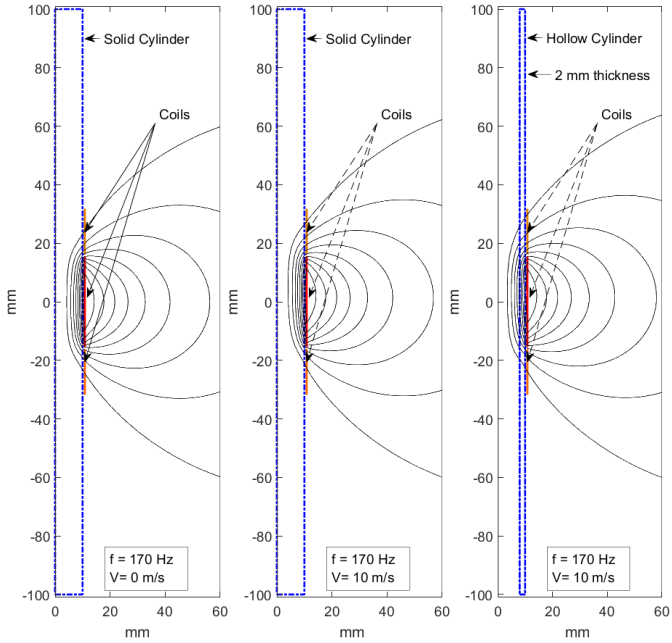

Fig. 5. Magnetic flux distribution at 170 Hz and 0 and 10 m/s with a solid cylinder and hollow cylinder

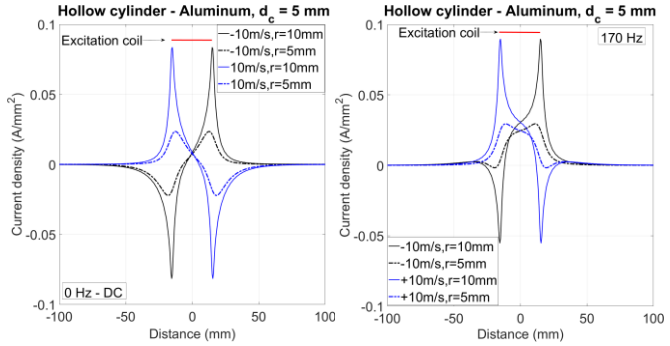

Fig. 6. Eddy current density on the surface hollow cylinder (r = 10 mm) and 5 mm beneath the surface (r = 5 mm) at DC excitation and AC excitation, 170 Hz and at speed, ±10 m/s

Fig. 5 presents magnetic flux distributions at zero speed and nonzero speed for solid cylinder and hollow cylinder models using analytical modeling. The speed effect causes magnetic flux to become unsymmetrical in comparison with symmetrical magnetic flux distribution at zero speed. The eddy current density graph on the surface of hollow cylinder and 5 mm beneath of cylinder surface is shown in Fig. 6 at ±10 m/s for DC and 170 Hz. The asymmetricity of eddy current density graph is apparent and it is caused by motional component of eddy current.

D. Parametric Analysis

Fig. 7 presents induced voltage of antiserially connected pickup coils versus frequency at 1 m/s and 2 m/s for aluminum and brass solid cylinders and hollow aluminum cylinders, which shows high frequency-dependency. All curves show a maximum value at different frequencies. The corresponding frequencies for maximum values of induced voltage are 300 Hz and 560 Hz for aluminum solid cylinder and brass solid cylinder, respectively. And they are 320 Hz, 620 Hz, 720 Hz, and 1060 Hz for hollow cylinders with shell thickness 5 mm, 2 mm, 1.5 mm, and 1 mm, respectively.

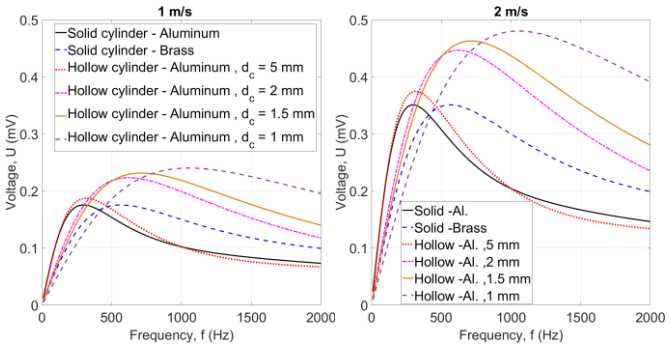

Fig. 7. Induced voltage (amplitude) versus frequency with various moving solid and hollow cylinders at 1 m/s and 2 m/s – Analytical

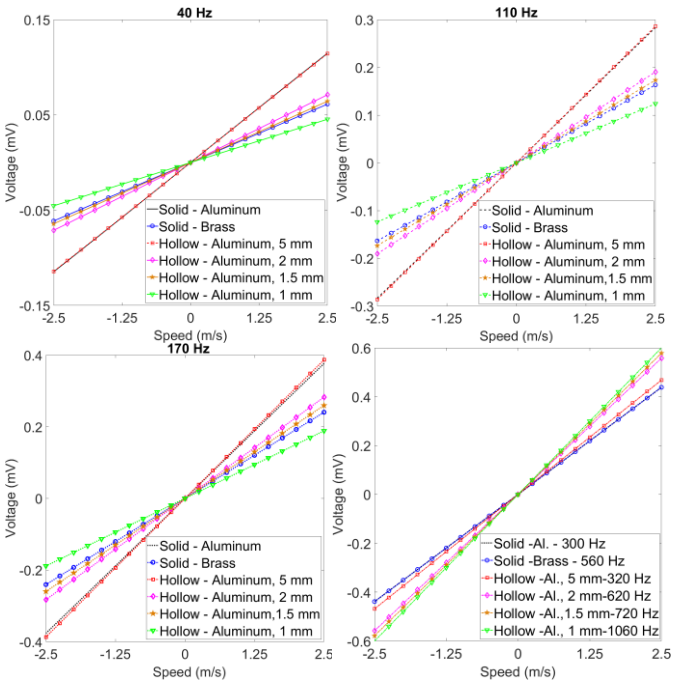

Fig. 8. Induced voltage, U (amplitude) versus speed, V with various moving solid and hollow cylinders at different excitation frequencies, I = 0.169 A-Analytical

Table 4
Sensitivity coefficients for amplitude of voltage, K'_A (μV/m/s)

Case	40 Hz	110 Hz	170 Hz	f_{max}
Solid cylinder Aluminum	46.0	113.5	150.7	300 Hz 175.5
Solid cylinder Brass	24.5	65.4	96.2	560 Hz 175.4
Hollow cylinder Aluminum, d_c = 5.0 mm	45.8	114.6	154.8	320 Hz 187.3
Hollow cylinder Aluminum, d_c = 2.0 mm	28.5	76.3	113.1	620 Hz 223.3
Hollow cylinder Aluminum, d_c = 1.5 mm	25.7	69.4	103.9	720 Hz 231.5
Hollow cylinder Aluminum, d_c = 1.0 mm	18.2	49.5	75.4	1060 Hz 240.1

The induced voltages of pickup coils versus speed at various frequencies are shown in Fig. 8 for solid and hollow cylinders. The induced voltage or the sensitivity, K' (U= $K' \cdot V$) is higher for an aluminum solid cylinder in comparison with brass solid

cylinder at same excitation frequency until 170 Hz as shown in Table 4. However, the sensitivities are the same at higher frequencies (300 Hz for aluminum and 560 Hz for brass) corresponding to the maximum value of induced voltages in Fig. 7. Induced voltage and sensitivity are lower with smaller shell thickness for hollow cylinders at the same excitation frequency until 170 Hz. The sensitivity increases with decreasing shell thickness for hollow cylinders at higher frequencies corresponding to maximum values of the induced voltage in Fig. 7. The induced voltage versus speed is a highly linear function, which could be utilized to estimate shell thickness from induced voltage value at different speeds.

Fig. 9 presents real (U_R) and imaginary (U_I) components of induced voltage for hollow cylinders. The real component of induced voltage is higher at higher excitation frequencies, which is the dominant component in comparison with the imaginary component. However, it is lower for lower frequencies, for example, at 40 Hz when corresponding sensitivities are compared, K'_R and K'_I ($U_R = K'_R \cdot V$, $U_I = K'_I \cdot V$) in Tables 5 and 6. Either real component or imaginary component of induced voltage versus speed has higher linearity. Therefore, it is more suitable to use real or imaginary components of voltage than the absolute value of the voltage at higher speeds, for example, up to 10 m/s [30]-[31], if experiments are performed at higher speeds than 2 m/s.

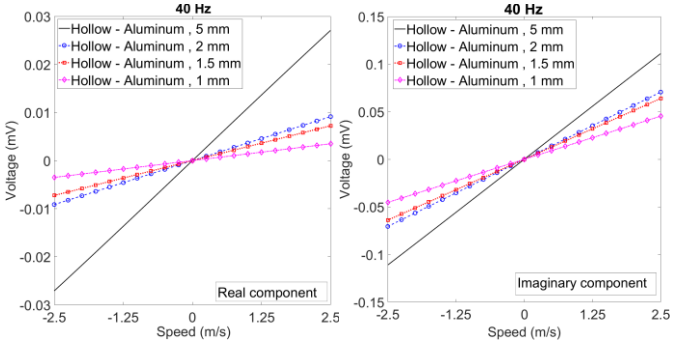

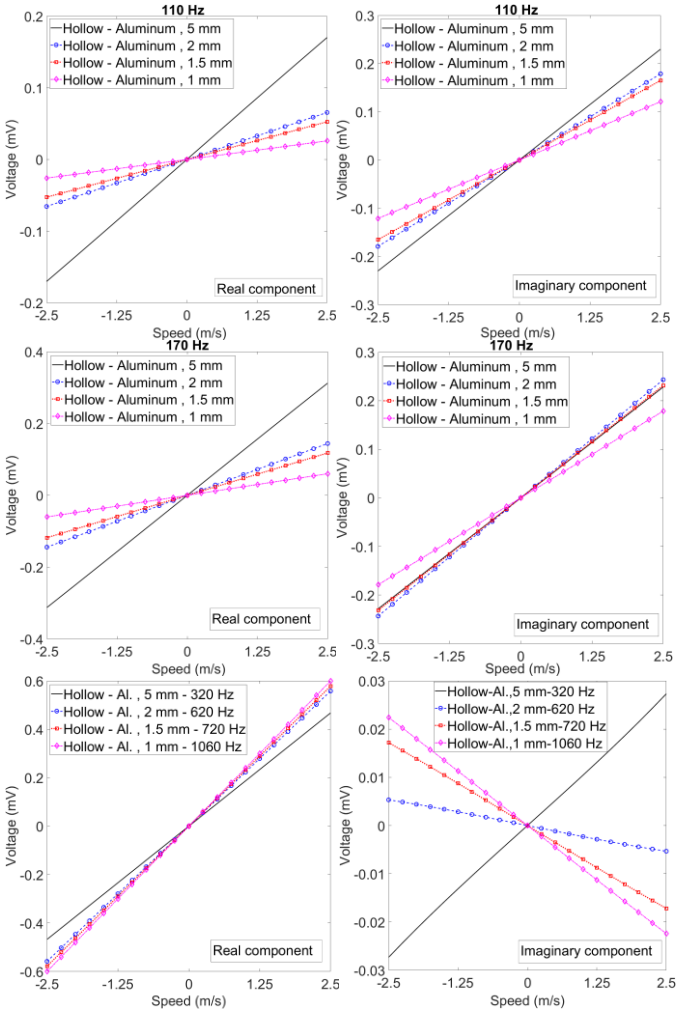

Fig. 9. Induced voltage, U (real and imaginary components) versus speed, V with various moving hollow cylinders at different excitation frequencies, I = 0.169 A- Analytical

Table 5
Sensitivity coefficients for real component of voltage, K'_R (μV/m/s)

Case	40 Hz	110 Hz	170 Hz	f_{max} Hz
Hollow cylinder Aluminum, d_c = 5.0 mm	10.9	68.3	125.1	320 Hz 187.0
Hollow cylinder Aluminum, d_c = 2.0 mm	3.7	26.3	57.7	620 Hz 223.3
Hollow cylinder Aluminum, d_c = 1.5 mm	2.9	21.1	47.2	720 Hz 231.3
Hollow cylinder Aluminum, d_c = 1.0 mm	1.4	10.4	24.1	1060 Hz 239.9

Table 6
Sensitivity coefficients for imaginary component of voltage, K'_I (μV/m/s)

Case	40 Hz	110 Hz	170 Hz	f_{max}
Hollow cylinder Aluminum, d_c = 5.0 mm	44.5	92.0	91.2	320 Hz 10.7
Hollow cylinder Aluminum, d_c = 2.0 mm	28.2	71.6	97.3	620 Hz -2.2
Hollow cylinder Aluminum, d_c = 1.5 mm	25.6	66.1	92.5	720 Hz -6.9
Hollow cylinder Aluminum, d_c = 1.0 mm	18.1	48.4	71.5	1060 Hz -9.0

The variations of induced voltage versus cylinder conductivity are shown in Fig. 10. The variations at lower frequencies and lower speed are almost linear, which can be utilized to estimate the conductivity of the cylinder. The maximum values of induced voltage appear at different conductivities, which depends on the excitation frequencies. For example, voltage maxima for 170 Hz is at conductivity, 57 MS/m and it is for 320 Hz at conductivity, 30 MS/m for hollow cylinder with 5 mm shell thickness. The maximum value of induced voltage is higher for hollow cylinders with smaller shell thickness.

The induced voltage is more sensitive to shell thickness below 5 mm and it is almost unchanged and a flat shape in larger shell thickness than 5 mm (Fig. 11). The sensitivity is higher at higher frequencies around 1000 Hz in comparison with 170 Hz and it increases with increasing conductivity. It is shown than the voltage of the sensor is monotonically increasing versus shell thickness up to 0.5 mm at 1000 Hz for different conductivities. However, it is monotonically increasing versus shell thickness up to 2 mm at 170 Hz. Therefore, shell thickness of hollow cylinder can be easily estimated up to 2 mm at 170 Hz and it is conceivable for higher shell thickness at lower excitation frequencies.

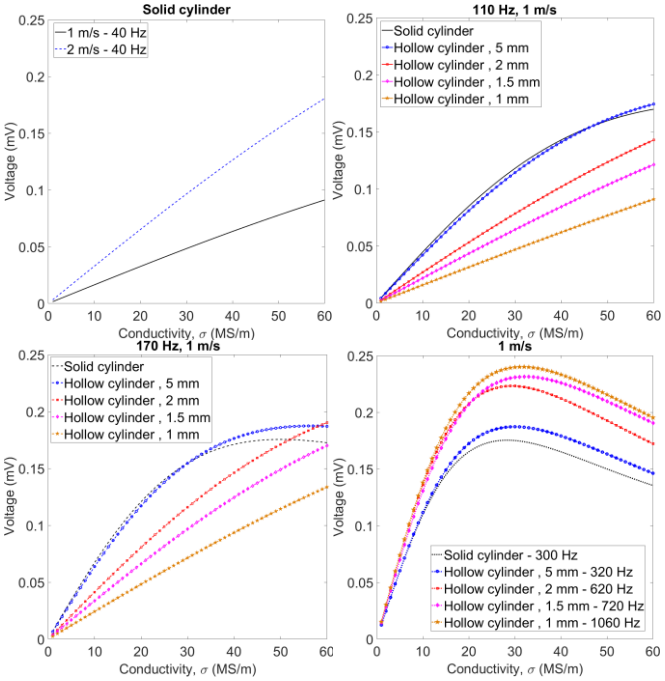

Fig. 10. Induced voltage (amplitude) versus conductivity with various moving solid and hollow cylinders at different excitation frequencies - Analytical

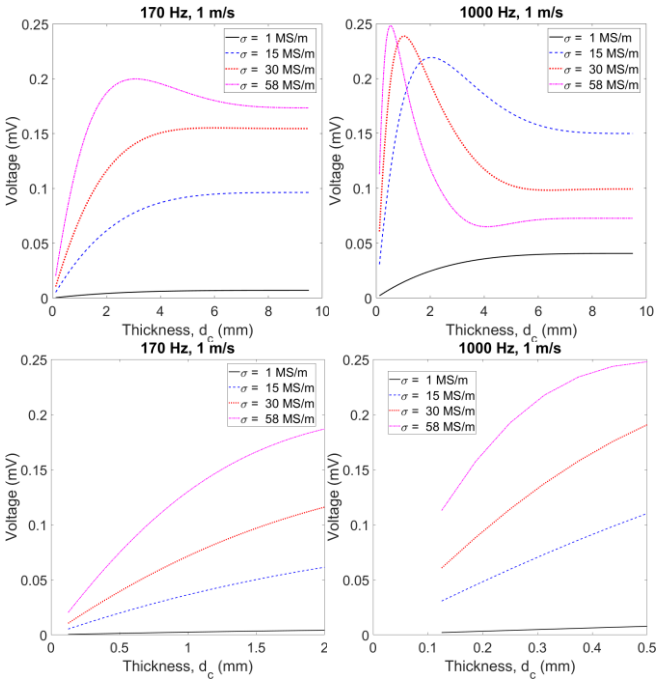

Fig. 11. Induced voltage (amplitude) versus hollow cylinder shell thickness with different conductivity at 1 m/s and 170 Hz and 1000 Hz

E. Comparison with FEM

Table 4 presents the comparison between analytical results and finite element method (FEM) using Maxwell software [32] with steady-state and constant speed, which shows compatible results. The maximum difference in percentage is 2.6%. The small differences between analytical and FEM results are mainly caused by numerical errors due to the slide mesh method concerning speed consideration in the FEM model.

Pick up coils voltage, $U_p(t)$ is calculated in (28) and (29). Second term in (29) is negligible in comparison with first term. Because time variation of current is proportional to ω ($=2\pi f$) and it is considerably higher than time variation of speed, $\partial V(t)/\partial t$ [25]-[26]. Therefore, simplified equation (30) is used to calculate pickup coils voltage for analytical method, $U_p(t)$ at transient and variable speeds, $V(t)$. Parameter, $K(f)$ is sensitivity factor per 1 (A) excitation coil current amplitude, which is a function of excitation frequency, f and depends on cylinder conductivity and shell thickness. The comparison between FEM and analytical results at variable speeds is shown in Fig. 12, in which analytical method results show excellent coincidence with FEM at variable speeds.

$$U_p(t) = -\frac{d\Psi_p}{dt}, \qquad \Psi_p \propto I \cdot \cos(\omega t) \cdot V(t) \tag{28}$$

$$U_p(t) \propto \omega \cdot I \cdot \sin(\omega t) \cdot V(t) - I \cdot \cos(\omega t) \cdot \frac{\partial V(t)}{\partial t} \tag{29}$$

$$U_p(t) = K(f) \cdot I \cdot \sin(\omega t) \cdot V(t) \tag{30}$$

Table 4
Comparison between analytical and FEM for voltage amplitude – 170 Hz

Case		Analytical, μV	FEM, μV
Solid cylinder Aluminum	1 m/s	150.8 (102.6%)	147.0 (100%)
	2 m/s	301.3 (102.5%)	294.0 (100%)
Solid cylinder Brass	1 m/s	96.3 (101.6%)	94.8 (100%)
	2 m/s	192.5 (101.4%)	189.8 (100%)
Hollow cylinder Aluminum, d_c = 5.0 mm	1 m/s	155.0 (102.6%)	151.1 (100%)
	2 m/s	309.6 (102.5%)	302.2 (100%)
Hollow cylinder Aluminum, d_c = 2.0 mm	1 m/s	113.2 (102.1%)	110.9 (100%)
	2 m/s	226.2 (102.1%)	221.6 (100%)
Hollow cylinder Aluminum, d_c = 1.5 mm	1 m/s	103.9 (102.1%)	101.8 (100%)
	2 m/s	207.7 (101.2%)	205.2 (100%)
Hollow cylinder Aluminum, d_c = 1.0 mm	1 m/s	75.4 (101.3%)	74.4 (100%)
	2 m/s	150.8 (100.9%)	149.5 (100%)

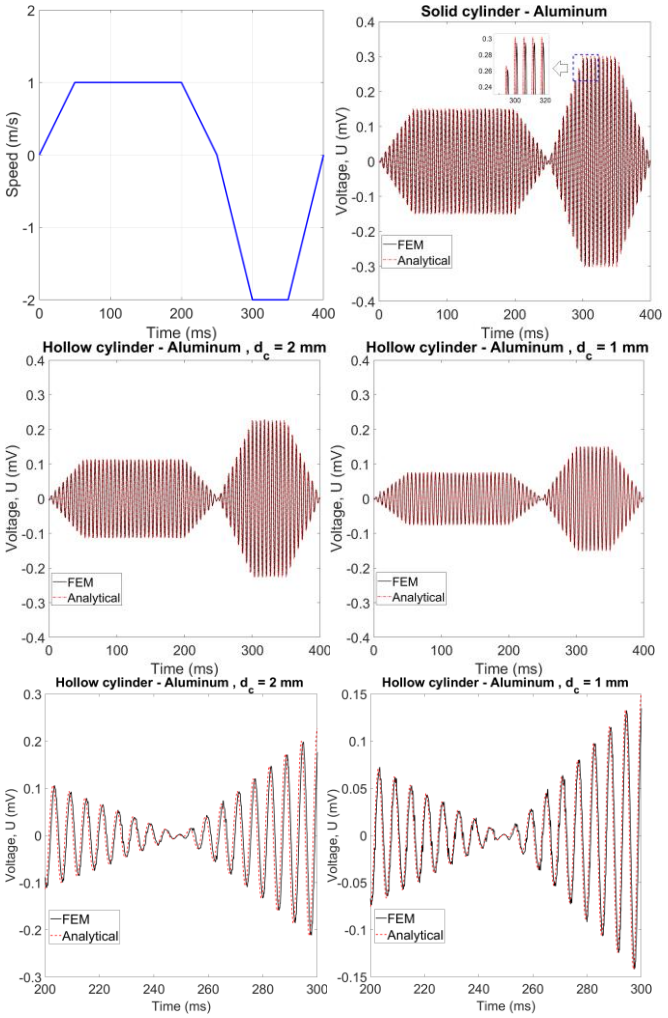

Fig. 12. Voltage versus time (0 - 400 ms) at given speed profile – comparison between analytical and FEM at excitation frequency, f = 170 Hz (it is also zoomed between 200 - 300 ms for hollow cylinders with d_c = 2 mm and 1 mm)

IV. Measurements

Experimental setup and measurement devices are shown in Fig. 13 and Fig. 14. The excitation coil and two pickup coils in the sensor, a digital oscilloscope, and a signal generator are used for the measurements. The excitation coil is supplied with the signal generator with an internal resistance of 50 Ω and a voltage amplitude of 10 V at different frequencies.

The relative instantaneous positions of the coils and the cylinder are measured by a potentiometric linear position sensor. The relative speed of the sensor is calculated numerically using the differentiation of relative positions of the moving part and the coils versus time [25]. The instantaneous pickup coil voltage and relative positions of the cylinder and the coils are saved by the digital oscilloscope as shown in Fig. 14.

The experimental results for induced voltages at 110 Hz and 170 Hz and variable speeds are shown in Fig. 15 - Fig. 20 in comparison with analytical calculations, which analytical induced voltages are compatible with experimental results. The speed profile is reciprocating, and the maximum applied speed varies between 1.5 m/s to 2.0 m/s. The biggest difference between analytical and experimental is shown in Fig. 17 for a hollow cylinder with 5 mm shell thickness at speed about 1.75 m/s, which is probably caused: firstly because of not exact measured conductivity used in the analytical method and secondly due to the not perfect symmetrical coupling between two pickup coils and excitation coil during measurements at speeds higher than 1.5 m/s. Also, imperfect shell thickness throughout the hollow cylinder length could be a reason for the mismatch between analytical and experimental results. Smaller differences are shown in Fig. 18 and Fig. 19. However, the differences are much less in Fig. 20 for a hollow cylinder with 1 mm thickness. The measured induced voltage reduces with decreasing shell thickness of hollow cylinder from 5 mm to 1 mm at 170 Hz in the same speed range, which experimentally proves the proposed method for shell thickness measurement of hollow cylinder as shown in Fig. 11.

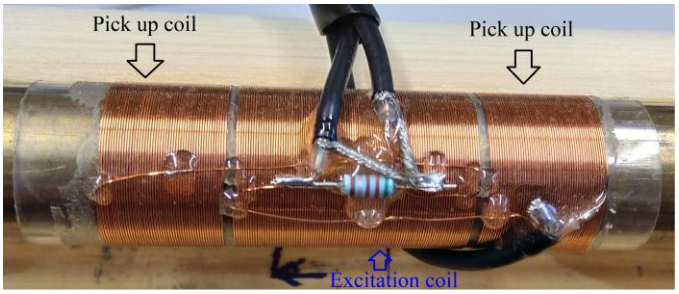

Fig. 13. Experimental coils arrangement - sensor

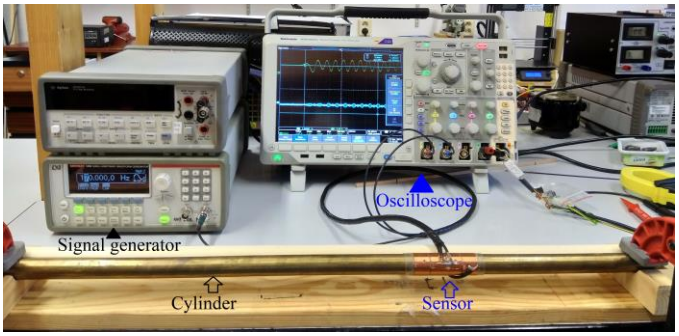

Fig. 14. Experimental setup – moving cylinder, sensor, signal generator, and oscilloscope

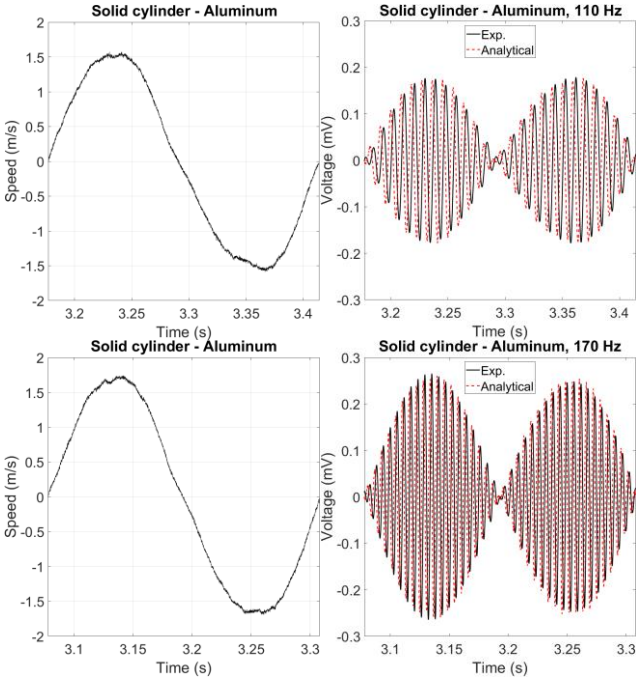

Fig. 15. Voltage versus time at measured speed profile for solid aluminum cylinder (D_o= 20 mm) – comparison between analytical and experimental, 110 Hz and 170 Hz

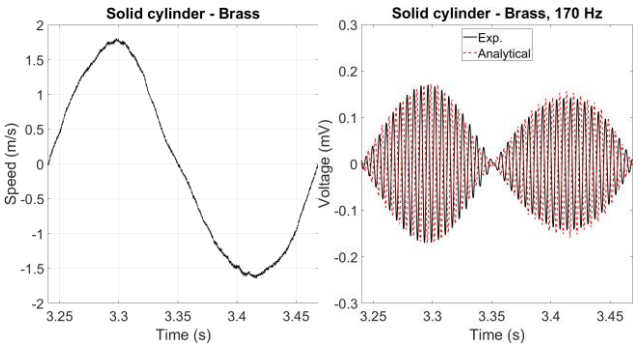

Fig. 16. Voltage versus time at measured speed profile for solid brass cylinder (D_o= 20 mm) – comparison between analytical and experimental, 170 Hz

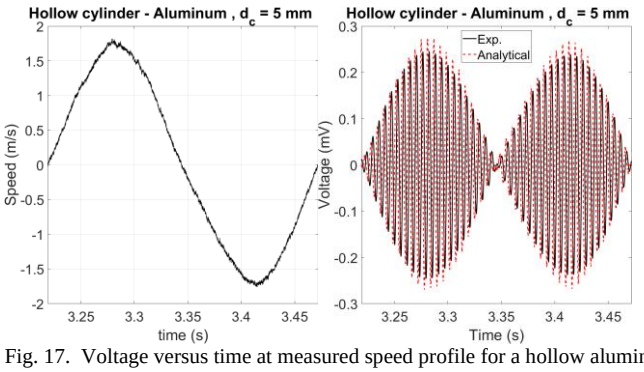

Fig. 17. Voltage versus time at measured speed profile for a hollow aluminum cylinder (D_o= 20 mm) with shell thickness, d_c = 5 mm– comparison between analytical and experimental, 170 Hz

Table 7 presents the comparison between analytical calculations and experimental results at 1 m/s and 1.5 m/s, which shows maximum error about 4%. Both experimental and analytical results for sensor voltage decrease with decreasing shell thickness from 2 mm to 1 mm. It is apparent that the shell thickness can be measured by the proposed method and using sensor output voltage in this paper. The comparisons are for hollow cylinders with shell thickness 2 mm, 1.5 mm and 1 mm. The same difference range can be observed for solid cylinders and hollow cylinder with shell thickness 5 mm. The measured induced voltage was measured at variable speeds; however, constant speed can be used for longer cylinders.

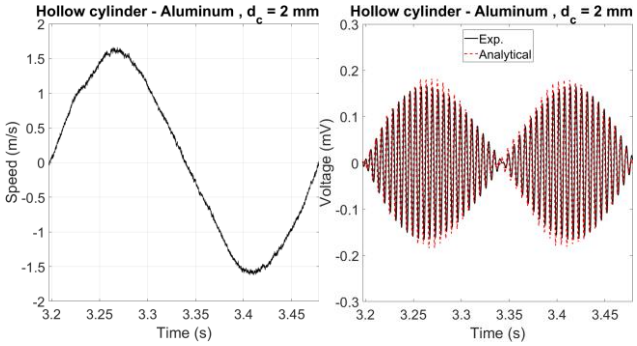

Fig. 18. Voltage versus time at measured speed profile for a hollow aluminum cylinder (D_o= 20 mm) with shell thickness, d_c = 2 mm– comparison between analytical and experimental, 170 Hz

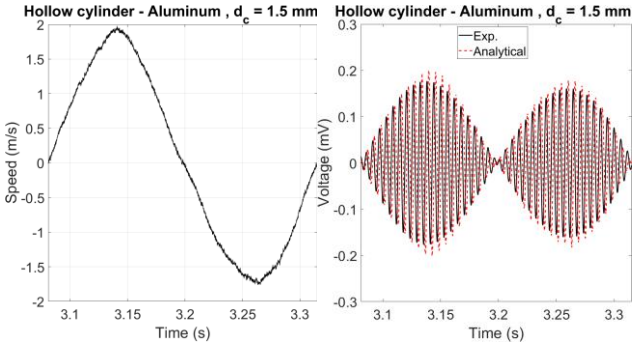

Fig. 19. Voltage versus time at measured speed profile for a hollow aluminum cylinder (D_o= 20 mm) with shell thickness, d_c = 1.5 mm– comparison between analytical and experimental, 170 Hz

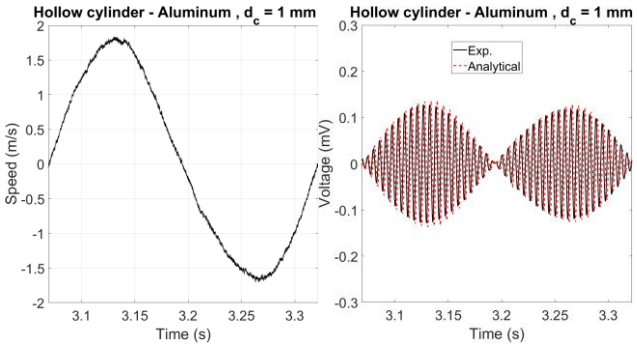

Fig. 20. Voltage versus time at measured speed profile for a hollow aluminum cylinder (D_o= 20 mm) with shell thickness, d_c = 1 mm– comparison between analytical and experimental, 170 Hz

Table 7
Experimental and analytical results for amplitude of voltage (mV) - 170 Hz

Case	d_c = 2.0 mm	d_c = 1.5 mm	d_c = 1.0 mm
Exp.,+1.5 m/s	0.1627(100%)	0.1542(100%)	0.1131(100%)
Ana.,+1.5 m/s	0.1697(104%)	0.1558(101%)	0.1131(100%)
Exp.,+1.0 m/s	0.1126(100%)	0.1059(100%)	0.0722(100%)
Ana.,+1.0 m/s	0.1132(101%)	0.1039(98%)	0.07543(104%)

V. Smaller Diameter Hollow Cylinder

Smaller diameter cylinder with 18 mm diameter and shell thickness 2 mm with same speed sensor is also theoretically and experimentally investigated. Zero eccentricity or misalignment, 0.5 mm and 0.75 mm radial eccentricity are considered as shown in Fig. 21. Time stepping 3D FEM is used for eccentricity modeling and the results are shown in Table 8. The maximum difference between without eccentricity and 0.75 mm eccentricity is as small as 2.3%, which can be also caused by numerical error in 3D FEM because of sliding mesh used for the motion modeling.

The comparison between analytical calculations without consideration of eccentricity and experimental results with 0.5 mm eccentricity are shown in Fig. 22 and Fig. 23 at 110 Hz and 170 Hz. The results match well as 20 mm diameter hollow cylinders (Fig.17-Fig.20), which negligible eccentricity or misalignment effects supposition can be accomplished.

Table 8
Comparison between without and without eccentricity using 2D analytical and 3D FEM analysis – 170 Hz, 1m/s

Case	Analytical, μV	3D FEM, μV
Without eccentricity	84.482 (102.65%)	82.3046 (100%)
With eccentricity 0.5 mm	-	81.8568 (99.46%)
With eccentricity 0.75 mm	-	84.2296 (102.34%)

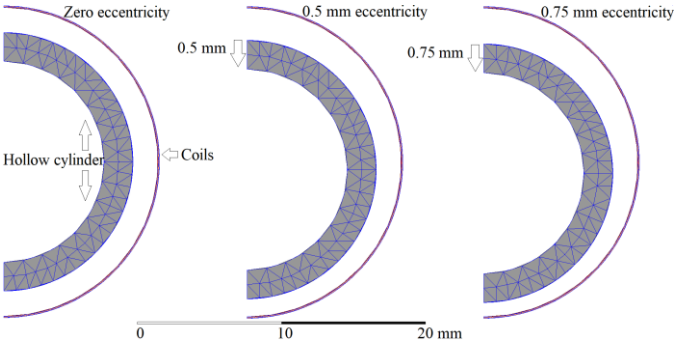

Fig. 21. Eccentricity modeling in 3D FEM– 18 mm diameter hollow cylinder with 2 mm shell thickness is shifted perpendicularly to translational motion direction

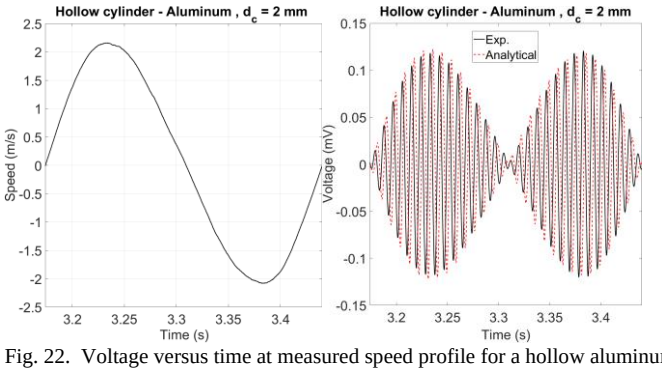

Fig. 22. Voltage versus time at measured speed profile for a hollow aluminum cylinder with outer diameter, D_o= 18 mm and shell thickness, d_c = 2 mm– comparison between analytical and experimental with 0.5 mm misalignment, 110 Hz

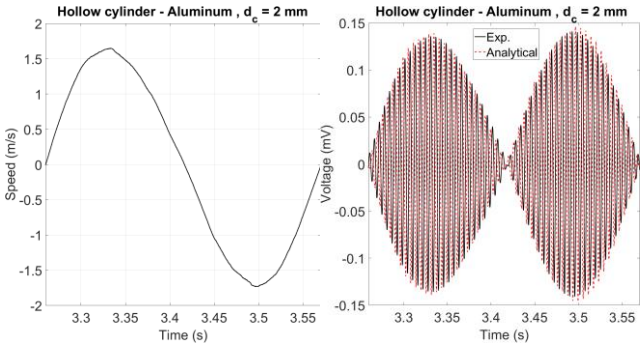

Fig. 23. Voltage versus time at measured speed profile for a hollow aluminum cylinder with outer diameter, D_o= 18 mm and shell thickness, d_c = 2 mm– comparison between analytical and experimental with 0.5 mm misalignment, 170 Hz

VI. Discussions

Spatial resolution of the proposed method and sensor depends on the excitation frequency and speed. For example, spatial resolution is 5.9 mm at 170 Hz and 1 m/s with measuring sensor voltage output using rms reader for each period of excitation frequency. Spatial resolution can be reduced with increasing frequency and reducing speed.

The voltage peaks, the rms voltage, or the rectified DC value in each half period can be used to calculate shell thickness of nonmagnetic hollow cylinders when the absolute value of induced voltage is used for shell thickness estimation. Single-chip synchronous detector with similar performance as lock-in amplifier, for example, AD630 modulator/demodulator IC can be used for the output voltage processing when real and imaginary components of induced voltages are used for shell thickness estimation. The use of DSP lock in amplifier would certainly contribute to a more efficient postprocessing of useful signals when the speed is constant in the test. However, standard lock in amplifier can be less practical for tests at variable speeds concerning time delay caused by output filter. Variable speed operation of the sensors was performed in this paper as used aluminum cylinders are short with 700 mm length. Using static eddy current nondestructive is not suitable for fast and high speed tests as the motional component of induced eddy current can cause nonnegligible errors in the test results [18]-[19]. Operation of the sensor with constant speed for longer cylinders is planned works for the future.

We used speed component of eddy current to estimate hollow cylinder shell thickness. It is assumed that speed, conductivity and outer diameter of cylinder are known values. If speed, conductivity and outer diameter of hollow cylinders are not known, single frequency test is not enough and it is needed to test with 4-5 frequencies (could be simultaneously or separately and to be measured with lock-in amplifier), which are standard procedure to estimate more unknowns. It can be proposed another vertical sensor to help estimating, for example, outer diameter of cylinders or other unknown parameters. Using additional sensors is a common method to find more unknowns as presented in [4], which two sensors or measuring systems were used to solve liftoff problem.

The proposed method in this paper could be implemented for magnetic steel pipes for different industry applications and

nonmagnetic hollow cylinders and plates to estimate thickness and detect surface and subsurface flaws and defects [33]-[36].

VII. Conclusions

The thickness evaluation of nonmagnetic hollow cylinders using motional component of induced eddy currents in the hollow cylinders shell was presented in this paper. Thickness measurement of cylinder shell with high speed is possible using the method presented in this paper. The main advantage of proposed method in this paper is fast and easy estimation of shell thickness of hollow cylinders and pipes with consideration of the speed effects.

Effects of the motional component of induced eddy current in the conductive cylinder were utilized as the induced voltage in pickup coils to measure shell thickness. A novel analytical method was presented to evaluate induced motional eddy current for shell thickness estimation. Parametric analysis for different frequencies, shell thicknesses, speeds, and materials conductivity was performed using the analytical method. Comparison between analytical method and time stepping FEM shows high accuracy of the proposed analytical method at constant and variable speeds versus time. The measurements correspond well with theoretical results for solid and hollow cylinders. Therefore, utilizing a motional eddy current is an appropriate method for shell thickness estimation in hollow cylinders.

The power consumption of the excitation coil is 53 mW. The sensitivity could be increased with a higher number of turns, which is only limited by parasitic capacitance. Optimization of an excitation coil and pickup coils in terms of their configuration, dimensions, number of turns to achieve maximum sensitivity to power consumption ratio are planned for future works. The experimental and theoretical works for hollow cylinders with bigger outer diameter will be considered as the next works to evaluate the effectiveness of the proposed method for different sizes of hollow cylinders and pipes.

Appendix

A. Assumptions and generic formulation

1- There is a universal bulk speed of material in a direction such that $\nabla(\mathrm{V}\cdot A)=0$. A is magnetic vector potential.

2- The speed is low in comparison to the speed of light.

3- The Ohm's law is assumed in a form $J=\mu_0\sigma[E+V\times B]$.

4- Motional effects on permittivity and permeability are neglected.

5- Vacuum permittivity and permeability is assumed everywhere.

6- Displacement current is neglected.

7- Time-varying but stationary current distribution is assumed.

8- The capacity effects can be neglected ρ, ϕ = 0.

9- The operation frequency is low enough that the presence of pick-up coils does not affect the field distribution.

10- Current density is stationary and satisfies $\nabla\cdot J=0$ at every point.

11- Coulomb gauge for magnetic vector potential is used.

12- Under these assumptions the general partial differential equation is described via:

$$\nabla^2 A-\mu_0\sigma\left(\frac{\partial A}{\partial t}-V\times(\nabla\times A)\right)=-\mu_0 J_s \quad (31)$$

which is further simplified into:

$$\nabla^2 A-\mu_0\sigma\left(\frac{\partial A}{\partial t}+(V\cdot\nabla)A\right)=-\mu_0 J_s \quad (32)$$

With J_s is the source current density substituting the excitation coil.

References

[1] N. Bowler, Eddy-current nondestructive evaluation. New York: Springer; 2019.

[2] W. Yin, A. J. Peyton, Thickness measurement of non-magnetic plates using multi-frequency eddy current sensors. NDT&E Int 40 (2007) 43-48

[3] W. Yin, K. Xu, A Novel Triple-Coil Electromagnetic Sensor for Thickness Measurement Immune to Lift-Off Variations. IEEE Trans. Instr. Meas. 65(1) (2016) 164-169

[4] J. R. Salas Avila, M. Lu, R. Huang, Z. Chen, S. Zhu S, W. Yin, Accurate measurements of plate thickness with variable lift-off using a combined inductive and capacitive sensor. NDT&E Int. 110 (2020) 102202

[5] X. Chen, Y. Lei, Excitation current waveform for eddy current testing on the thickness of ferromagnetic plates. NDT&E Int. 66 (2014) 28-33

[6] S. Yoshioka, Y. Gotoh, Proposal of thickness measurement method of steel plate with high liftoff using pulsed magnetic field. IEEE Trans. MAG. 53(11) (2017) 4400404

[7] A. E. Lakhdari, A. Cheriet, I. N. El-Ghoul, Skin effect based technique in eddy current non-destructive testing for thickness measurement of conductive material. IET Sci, Meas & Tech. 13(2) (2018) 255-259

[8] R. Huang, M. Lu, A. Peyton and W. Yin, Thickness measurement of metallic plates with finite planar dimension using eddy current method. IEEE Trans. Instr. Meas. 69(10) (2021) 8424-8431

[9] X. Mao, Y. Lei, Thickness measurement of metal pipe using swept-frequency eddy current testing. NDT&E Int. 78 (2016) 10-19

[10] N. Ulapane, A. Alempijevic, J. V. Miro, T. Vidal-Calleja, Non-destructive evaluation of ferromagnetic material thickness using pulsed eddy current sensor detector coil voltage decay rate. NDT&E Int. 100 (2018) 108-114

[11] X. Chen, J. Li, Z. Wang, Inversion method in pulsed eddy current testing for wall thickness of ferromagnetic pipes, IEEE Trans. Instr. Meas. 69(12) (2020) 9766 – 9773

[12] M. Tohara and Y. Gotoh, Inspection method of outer side defect in ferromagnetic steel tube by insertion-type electromagnetic sensor using square wave alternating magnetic field with DC bias. IEEE Trans. MAG. 57(2) (2021) 6200105

[13] S. Niikura and A. Kameari, Analysis of eddy current and force in conductors with motion. IEEE Trans. MAG. 28(2) (1992) 1450-1453

[14] Y. S. Sun, W. Lord, G. Katragadda, Y. K. Shin, Motion induced remote field eddy current effect in a magnetostatic non-destructive testing tool: a finite element prediction, IEEE Trans. MAG. 30(5) (1994) 3304-3307

[15] G. Katragadda, W. Lord, Y. S. Sun, S. Udpa, L. Udpa, Alternative magnetic flux leakage modalities for pipeline inspection. IEEE Trans. MAG. 32(3) (1996) 1581-1584

[16] S. Yang, Y. Sun, L. Udpa, S. S. Udpa, W. Lord, 3D simulation of velocity induced fields for nondestructive evaluation application, IEEE Trans. MAG., 35(3) 1999 1754-1756

[17] W. Yin, A. J. Peyton, Sensitivity formulation including velocity effects for electromagnetic induction systems, IEEE Trans. MAG. 46(5) 2010 1172-1176

[18] G. Piao, J. Li, L. Udpa, S. Udpa, and Y. Deng, The effect of motion-induced eddy currents on three-axis MFL signals for high-speed rail inspection. IEEE Trans. MAG. 57(4) (2021) 6200211

[19] F. Yuan, Y. Yu, L. Li, and G. Tian, Investigation of DC electromagnetic-based motion induced eddy current on NDT for crack detection. IEEE SENS. J. 21(6) (2021) 7449-7457

[20] F. Yuan, Y. Yu, W. Wang and G. Tian, A novel probe of DC electromagnetic NDT based on drag effect: design and application in crack characterization of high-speed moving ferromagnetic material. IEEE Trans. Instr. Meas. 70 (2021) 6006210

[21] C. C. Feng, W. E. Deeds, C. V. Dodd, Analysis of eddy-current flowmeters, J App. Phys. 46(7) 1975 2935-2940
[22] A. H. Kahn, M. L. Mester, Through-transmission impedance measurements on moving metallic sheets, Rev. Prog Quan Nondest Eval. 11 (1992) 249-255
[23] T. Itaya, K. Ishida, A. Tanaka, N. Takehira, T. Miki, Analysis of a fork-shaped rectangular coil oriented perpendicular to moving conductor slabs. NDT&E Int. 44 (2011) 413-420.
[24] K. Ishida, T. Itaya, A. Tanaka, N. Takehira, T. Miki, Thickness measurement of moving nonmagnetic metal foil by impedance variation. Elect. Eng. in Japan, 180 (2012) 15-23.
[25] M. Mirzaei, P. Ripka, A. Chirtsov, J. Vyhnanek, V. Grim, Design and modeling of a linear speed sensor with a flat type structure and air coils. J. Magnetism and Mag. Mater. 495 (2020) 165834
[26] M. Mirzaei, P. Ripka, A. Chirtsov, J. Vyhnanek, Eddy current linear speed sensor, IEEE Trans. Mag., 55(1) (2019) 4000304
[27] K. Ishida, T. Itaya, A. Tanaka, N. Takehira, Exact analysis of a linear velocity sensor, IEEE Trans. Inst. Meas. 70 (2020) 6002106
[28] C. V. Dodd, W. E. Deeds, Analytical solutions to eddy-current probe-coil problems, J. App. Phys. 39(6) (1968) 2829-2838
[29] K. J. Binns, P. J. Lawrenson, and C. W. Trowbridge, The analytical and numerical solutions of electric and magnetic fields, Chichester England, New York: John Wiley & Sons Ltd; 1992.
[30] M. Mirzaei, P. Ripka, and V. Grim, A novel eddy current speed sensor with a Ferrite E-core, IEEE Mag. Lett., 11(1) (2020) 8102905
[31] M. Mirzaei, P. Ripka, A. Chirtsov, and V. Grim, Eddy current speed sensor with magnetic shielding, J. Magnetism and Mag. Mater., 502 (2020) 166568
[32] Ansys/maxwell (Ansoft), https://www.ansys.com/products/electronics/ansys-maxwell, Accessed on 04.06.2021 [Online]
[33] S. She, Y. Chen, Y. He, Z. Zhou, X. Zou, Optimal design of remote field eddy current testing probe for ferromagnetic pipeline inspection, Measurement, 168 (2021) 108306
[34] C. S. Angani, H. G. Ramos, A. L. Ribeiro, T. J. Rocha, Evaluation of transient eddy current oscillations response for thickness measurement of stainless steel plate, Measurement, 90 (2016) 59-63
[35] K. S. Rao, S. Mahadevan, B. P. Chandra Rao, S. Thirunavukkarasu, A new approach to increase the subsurface flaw detection capability of pulsed eddy current technique, Measurement, 128 (2018) 516-526
[36] T. J. Rocha, H. G. Ramos, A. L. Ribeiro, D. J. Pasadas, C. S. Angani, Studies to optimize the probe response for velocity induced eddy current testing in aluminium, Measurement, 67 (2015) 108-115